

Ru–CeO₂ and Ni–CeO₂ Coated on Open-Cell Metallic Foams by Electrodeposition for the CO₂ Methanation

Phuoc Hoang Ho,^{||} Giancosimo Sanghez de Luna,^{||} Arturo Poggi, Monica Nota, Enrique Rodríguez-Castellón, Giuseppe Fornasari, Angelo Vaccari, and Patricia Benito*

Cite This: *Ind. Eng. Chem. Res.* 2021, 60, 6730–6741

Read Online

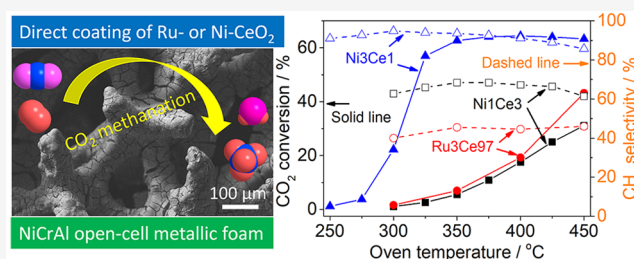
ACCESS |

Metrics & More

Article Recommendations

Supporting Information

ABSTRACT: CO₂ methanation structured catalysts, made by a layer of Ru–CeO₂ or Ni–CeO₂ (Ru/Ce = 3/97; Ni/Ce = 1/3 and 3/1) on open-cell NiCrAl foams, are prepared by electrodeposition and a subsequent calcination step. The performance of the catalysts at a space velocity of 320,000 mL g_{cat}⁻¹ h⁻¹ in a feedstock with H₂/CO₂/N₂ = 4/1/1 v/v, significantly depends on the Ni content and the preparation method. A low Ru or Ni content promotes the metal–CeO₂ interaction, the formation of defects in CeO₂ as well as the development of a lower amount of cracks in the coating; however, the catalysts show a poor CO₂ conversion and selectivity to CH₄. The CH₄ production rate at low temperature largely increases for the high Ni loaded catalyst, 68.7 L_{CH₄} g_{Ni}⁻¹ h⁻¹ at 350 °C oven temperature. This productivity is similar to the value obtained with a Ni₃Ce₁ pellet catalyst prepared by the coprecipitation method, a behavior not achievable for low Ru- and Ni-loaded catalysts.



1. INTRODUCTION

Synthetic natural gas is obtained by the valorisation of CO₂ with H₂, coming from water electrolysis powered by renewable energies, the so-called Power-to-Gas (PtG).¹ This process has been demonstrated, and both research and pilot plants are under operation.² However, there is still room for improvement in some aspects of the thermocatalytic CO₂ methanation, such as the development of catalysts active at low temperature and heat management.³ Structured catalysts based on metallic supports enhance the heat (and mass) transfer in the exothermic hydrogenation of CO₂ to CH₄, of paramount importance to control the composition at the outlet of the reactor.⁴ The active Ni- and Ru-based methanation catalysts (e.g., Ni/Al₂O₃, Ni/CeO₂, Ni–CeO₂–ZrO₂, Ni(X)AlO_x (X = La, Ce, Y), Ru–Ni/MgAl₂O₄) have been coated on Al honeycomb, FeCrAlloy micromonoliths, AISI microchannels, as well as on Ni, Al, and NiCrAl foams.^{5–13} The catalytic performance and heat management of the structured catalytic beds depend on the properties of both coating and support. For instance, Ni/CeO₂ catalysts coated on Al honeycomb fin supports, with optimized cell density and configuration of the fin, generate a moderate hot spot under industrial-type conditions.^{8,9}

Ni/CeO₂ catalysts outperform the classical Ni/Al₂O₃ system,^{14–16} Ni on a basic La₂O₃ support,¹⁷ and on other types of supports such as ZrO₂, TiO₂, and SiO₂.¹⁸ Similarly, an enhanced activity is reported for Ru/CeO₂,^{19,20} though it has been less investigated for the CO₂ methanation. The advantages of CeO₂ as a support are correlated to oxygen

vacancies and ceria reducibility.²¹ The reduced and basic ceria surface promotes the CO₂ adsorption and decomposition, while the oxygen vacancies catalyze the formation and dissociation of reaction intermediates. Furthermore, the metal–support interaction determines the properties of both the metal (e.g., reducibility, particle size, sintering) and CeO₂ species (vacancies) and, consequently, the H₂ and CO₂ activation. For instance, the mechanism of CO₂ methanation over Ru-substituted CeO₂ and Ru supported on CeO₂ is different.²² This could be related to the weakening of the Ce–O bond strength in the former, due to the doping of Ru into CeO₂ lattice, generating more oxygen vacancies.²³ On the other hand, hexagonal Ni nanocrystallites on CeO₂ with a strong metal–oxide interaction facilitate the H₂ activation/dissociation and therefore the hydrogenation of CO₂, preferentially adsorbed/activated at the interface between Ni and CeO₂, to CH₄.²⁴ However, the decoration/encapsulation of Ni nanoparticles by a thin layer of reduced ceria can decrease the catalytic capacity for CO₂ activation/conversion. The selectivity of the methanation process has been related to metal loading and particle size. Low-loaded Ni catalysts are associated with a poor activity and selectivity to CH₄ due to

Special Issue: Enrico Tronconi Festschrift

Received: December 7, 2020

Revised: February 11, 2021

Accepted: February 13, 2021

Published: February 24, 2021



structural effects;²⁵ however, high Ni loadings may provoke the Ni particle growth. The restructuring of Ru in the presence of O₂ at low temperature changes the selectivity, and the redispersion of Ru favors the production of CO.²⁶ Hence, a careful tailoring of the properties of metal, CeO₂, and the metal-CeO₂ interface is required to achieve the expected catalyst improvement.^{19,27} This could be accomplished by selecting the preparation method, namely the support synthesis and metal incorporation.

The reverse microemulsion method produces NiO–CeO₂ mixed oxides with a controlled size that outperform impregnated samples, due to the surface area and highly reducible Ni–O–Ce species on the surface of the nanoparticles.²⁸ The low activity of conventionally impregnated samples is overcome by modifying the nickel species incorporation procedure. Highly dispersed nickel particles with strong metal–support interaction and Ni nanoparticles embedded in the pore walls of three-dimensional mesoporous CeO₂ are obtained by the citric acid assisted impregnation²⁹ and solution combustion,³⁰ respectively. Moreover, the incorporation of nickel by gas discharge plasma leads to a catalyst with a trade-off between active sites for H₂ splitting and CO₂ activation.³¹ In this catalyst, enriched Ni–CeO₂ interfacial sites and well-dispersed Ni particles operate synergistically to produce methane efficiently at low reaction temperatures. The preparation method also controls the ceria morphology, which modifies the oxygen vacancies and, consequently, the activity of Ni and Ru catalysts.^{32–35} The higher number of Ce³⁺ species in CeO₂ nanorods than nanocubes explains the higher performance of the former at a low temperature and low Ni loadings.³² However, the oxygen vacancies–activity relationship is not always straightforward. A strong metal–support interaction between Ni and Ce may have a negative impact on the CO₂ conversion at low temperatures.¹⁶ Moreover, the formation of oxygen vacancies promoted by Ru is CeO₂ morphology-dependent.³⁴ Recently, the engineering of the oxygen vacancies has been claimed by adding Y₂O₃ to NiO–CeO₂, the vacancies promote the direct dissociation of CO₂ and therefore greatly enhance the activity.³⁶

In the preparation of the structured catalysts, the aim is to combine the above-described properties of the CeO₂-based catalysts and those of the structured support; however, this task could be challenging since the former could be altered in the structured material. The dip-coating of an already prepared Ni–CeO₂ catalyst should be carried out into an acid-free catalyst dispersion to avoid modifications of the catalyst.³⁷ Alternatively, the catalyst could be in situ synthesized on the surface of the structured support, but mimicking the properties of conventionally prepared catalysts could be not tricky. A chemical conversion method, where pretreated aluminum structures react with an oxidizing solution of cerium chloride, generates a nano-CeO₂ coating.³⁸ Through the *in situ* Solution Combustion Deposition method, thin, uniform, and high-resistance catalytic layers of Ni/GDC (gallium-doped CeO₂) deposit on foams active for the CO₂ methanation.³⁹ We have proposed the electrodeposition to coat high pore density metal open-cell foams by a thin film of Pd–CeO₂ and CeO₂.^{40,41} The electrodeposition of single CeO₂ coatings is a facile and fast procedure, and the thickness of the coating and the CeO₂ particle size could be tailored.⁴¹ On the contrary, the preparation of Pd–CeO₂ electrodeposits is challenging; the selection of Pd metal precursors, potential, and time is

required, though not enough to avoid the formation of some Pd⁰ particles.⁴⁰ An alternative is the impregnation of the noble metal, e.g., Ru, on the electrodeposited CeO₂.¹³

This work aims to prepare in a single-step Ru–CeO₂ and Ni–CeO₂ catalytic coatings on NiCrAl open-cell foams with small cell size (450 μm) to achieve both methanation activity at low temperature and enhanced heat transfer. The precipitation of CeO₂ containing Ni and Ru is performed for the first time by electrodeposition, more precisely, by the electro-base generation method. For Ni-based catalysts, the Ni loading is also modified. The interaction and dispersion of the metal species with CeO₂ are investigated and correlated to the catalytic activity. To better highlight the ability of the catalysts to activate both CO₂ and H₂, and to deal with the heat generated, the hydrogenation of CO₂ to CH₄ over the structured catalysts is evaluated at high space velocity values (GHSV = 38,200 h⁻¹ or based on the mass of the coating 320,000 mL g_{cat}⁻¹ h⁻¹ (H₂/CO₂/N₂ = 4/1/1 v/v)), measuring the temperature profiles along the centerline of the catalytic bed. These temperature profiles provide valuable information on the hotspots along the catalytic bed in terms of location and the temperature increment (compared to the oven temperature); however, they are rarely reported. For comparison purposes, pelletized catalysts were prepared by conventional methods.

2. EXPERIMENTAL SECTION

2.1. Preparation of the Catalysts. Chemicals used in the experiments were nickel(II) nitrate hexahydrate (Sigma-Aldrich, 98.5%), cerium nitrate nonahydrate (Sigma-Aldrich, 99%), ruthenium(III) nitrosyl nitrate solution (Ru 1.5% w/v, diluted in nitric acid, Alfa Aesar), hydrochloric acid (Sigma-Aldrich, 37%), and ammonia solution (25%, Merck). The structured supports are NiCrAl open-cell foams (disks in a dimension of 10 mm diameter × 1.6 mm thickness, 450 μm cell size) supplied by Alantum. Bare foams were rinsed with acetone and subsequently with water. After that, they were dried at 40 °C for 24 h.

Before coating, the clean NiCrAl foam disks were pretreated in HCl 5 M for 15 min, followed by rinsing thoroughly in ultrapure water. Then, M/Ce (M = Ni or Ru) cerium-based materials were in situ coated on the foams by electro-base generation technique in a double compartment electrochemical flow cell connected with a potentiostat (Metrohm Autolab PGSTAT204, equipped with NOVA software). Detailed information on the cell configuration can be found elsewhere.¹² Information on electrolytes and synthesis conditions are described in Table 1.

The electrolyte containing Ru was adjusted to pH 3.8 using a concentrated NH₃ solution to suppress the electro-reduction

Table 1. Electrolytes and Synthesis Conditions Used in the Preparation of the Catalysts

catalyst	foam	electrolyte	conditions
CeO ₂	NiCrAl	Ce(NO ₃) ₃ , 0.1 M	-1.3 V vs SCE, 600 s
Ni1Ce3	NiCrAl	Ni(NO ₃) ₂ /Ce(NO ₃) ₃ = 1/3, 0.1 M	-1.3 V vs SCE, 600 s
Ni3Ce1	NiCrAl	Ni(NO ₃) ₂ /Ce(NO ₃) ₃ = 3/1, 0.1 M	-1.3 V vs SCE, 600 s
Ru3Ce97	NiCrAl	Ru(NO)(NO ₃) ₃ /Ce(NO ₃) ₃ = 3/97, 0.1 M	-1.2 V vs SCE, 600 s

of noble metal cations to metallic particles, as reported elsewhere.⁴² Note that the electrodeposition time was adjusted to avoid the clog of the pores of the foams due to the deposition of a large amount of the coating. After being coated, the foams were rinsed three times with ultrapure water, dried at 40 °C for 24 h, and then calcined in an oven at 600 °C (ramp 10 °C min⁻¹) for 6 h.

For comparison purposes, three powder samples (CeO₂, Ni1Ce3, and Ni3Ce1) with a similar composition as the electrodeposited catalysts were prepared by coprecipitation. A solution containing Ce(NO₃)₃ 0.1 M or a mixture of Ni(NO₃)₂ and Ce(NO₃)₃ (Ni/Ce = 1/3 or 3/1 molar ratio), with a total concentration of 0.1 M, was added dropwise into a solution of NaOH, and the pH was controlled at 9.0. The mixture was then stirred for 1 h and filtered and washed with distilled water. The solid was dried at 80 °C for 24 h and subsequently calcined, using the same conditions as for foam catalysts.

2.2. Characterization Techniques. X-ray diffraction (XRD) of the coating layer on the foam or of the powder samples was performed using a PANalytical X'Pert diffractometer equipped with a copper anode ($\lambda_{\text{mean}} = 0.15418$ nm) and a fast X'Celerator detector. A wide-angle diffractogram was collected over a 2θ range from 5 to 80° with a step size of 0.07° and counting time 60 s.

Morphology of the coating was characterized by scanning electron microscopy (SEM) coupled to energy dispersive spectrometry (EDS) using an EP EVO 50 Series Instrument (EVO ZEISS) equipped with an INCA X-act Penta FET Precision EDS microanalysis and INCA Microanalysis Suite Software (Oxford Instruments Analytical).

Micro-Raman measurements were performed in a Renishaw Raman Invia configured with a Leica DMLM microscope. The system was equipped with edge filters to cut Rayleigh scattering, monochromators (1800 lines/mm for Ar⁺ laser, and 1200 lines/mm for diode laser) and a charge-coupled device (CCD) thermoelectrically cooled (203 K) detector. Measurements were performed for the as-synthesized, calcined, and spent samples using the Ar⁺ Laser (514.5 nm) at a power of 3 mW (10% of maximum power level). Each spectrum was recorded with four accumulations (30 s for each). About six to nine measurements were performed at different locations on each sample.

The transmission electron analyses were performed with an FEI TECNAI F20 microscope operating at 200 kV. The instrument is also equipped with a dispersion microanalysis of energy (EDS) and the scanning electron microscopy (STEM) accessory. The coatings in the foams were carefully scratched using a scalpel and subsequently dispersed in isopropyl alcohol and sonicated for 45 min. One drop of the solution is then deposited on a perforated carbon film supported by a gold grid. The grid was then dried at 100 °C. The TEM images were taken in the phase contrast mode and Selected Area electron diffraction (SAED). STEM pictures were recorded using a High Angle Annular Dark Field (HAADF) detector.

X-ray photoelectron spectra (XPS) were recorded with a PHI VersaProbe II Scanning XPS Microprobe with scanning monochromatic X-ray Al K α radiation as the excitation source (100 μm area analyzed, 25.0 W, 15 kV, 1486.6 eV), and a charge neutralizer. The pressure in the analysis chamber was maintained lower than 2.0×10^{-6} Pa. High-resolution spectra were recorded at a given takeoff angle of 44° by a multichannel hemispherical electron analyzer operating in the constant pass

energy mode at 29.35 eV. Spectra were charge referenced with the C 1s of adventitious carbon at 284.8 eV. The energy scale was calibrated using Cu 2p_{3/2}, Ag 3d_{5/2}, and Au 4f_{7/2} photoelectron lines at 932.7, 368.2, and 83.9 eV, respectively. The Multipack software version 9.6.0.15 was employed to analyze in detail the recorded spectra. The obtained spectra were fitted using Gaussian–Lorentzian curves to more accurately extract the binding energies of the different element core levels.

Hydrogen temperature-programmed reduction (H₂-TPR) was carried out in an AutoChem II (Chemisorption analyzer, Micromeritics). The catalysts (two calcined coated foams containing about 20 mg of the coating or 100 mg of powder catalysts) were placed in a U-shape reactor (i.d. 10 mm) and pretreated at 150 °C under 30 mL min⁻¹ of He for 30 min. After that, the reactor was cooled down to 40 °C under He, and the carrier gas was switched to 5% H₂/Ar (v/v) at 30 mL min⁻¹. When the baseline was stable, the temperature was increased to 900 °C with a ramp of 10 °C min⁻¹. The effluent gas passed through an ice-cold trap, afterward, the H₂ consumption was measured using a thermal conductivity detector (TCD).

2.3. Catalytic Tests. The CO₂ methanation tests over structured catalysts were performed in a quartz reactor (ID 10.0 mm) loaded with three foam catalysts (approximately 4.8 mm in height). To measure the temperature profile, a 2 mm thermowell (quartz tube) was inserted into the middle of the catalytic bed. A thermocouple (K-type) can manually slide inside the thermowell allowing to measure the temperature along the length of the catalytic bed during the tests. The catalyst was reduced in 200 mL min⁻¹ of H₂/N₂ = 1/1 (v/v) at 600 °C for 2 h. After cooling to 250 °C and stabilizing at this temperature for 30 min in N₂, the feed gas (H₂/CO₂/N₂ = 4/1/1 v/v) with a total flow rate of 240 mL min⁻¹ was sent to the reactor. This condition generated a gas hourly space velocity (GHSV) of 38,200 h⁻¹ (GHSV = total flow rate/apparent volume of the foam bed). The reaction was carried out from 250 to 450 °C (or 600 °C in some tests) with an interval of 25 °C. The temperature was set to a defined value in N₂ atmosphere, once the temperature is reached (and it is stable, approximately 30 min each point) the reaction mixture was fed. After passing through a cold trap for water condensation, the outlet stream was analyzed online by a PerkinElmer Auto system XL gas chromatograph, equipped with two thermal conductivity detectors (TCD) and two Carbo-sphere columns using He as a carrier gas for CO, CH₄, and CO₂ quantification, and N₂ for H₂ analysis. Detailed information on the calculation of conversion and selectivity can be found in our previous work.¹²

The tests over the pelletized catalysts were performed keeping both the volume of the bed and the amount of catalyst constant in comparison to the ones over structured catalysts. Therefore, 45 mg of pelletized catalyst (Ni1Ce3 or Ni3Ce1) (similar to the amount of coating on 3 foams) was diluted with 470 mg of quartz (with the same particle size of the pellet, mesh 30–40) to have a 4.8 mm height bed.

The apparent activation energy (E_a) of each catalyst was calculated from the slope of the Arrhenius plot in the kinetically determined reaction temperature. The temperature values used were measured at the surface of the catalytic bed near the inlet, at which the conversion values of CO₂ were lower than 25% to minimize the effect of heat generation from

the reaction. Detailed information on the calculation can be found elsewhere.⁴³

3. RESULTS AND DISCUSSION

3.1. Characterization of As-Synthesized and Calcined Coated Foams. SEM images of the foams after electro-deposition and drying are shown in Figure 1. The layer of the

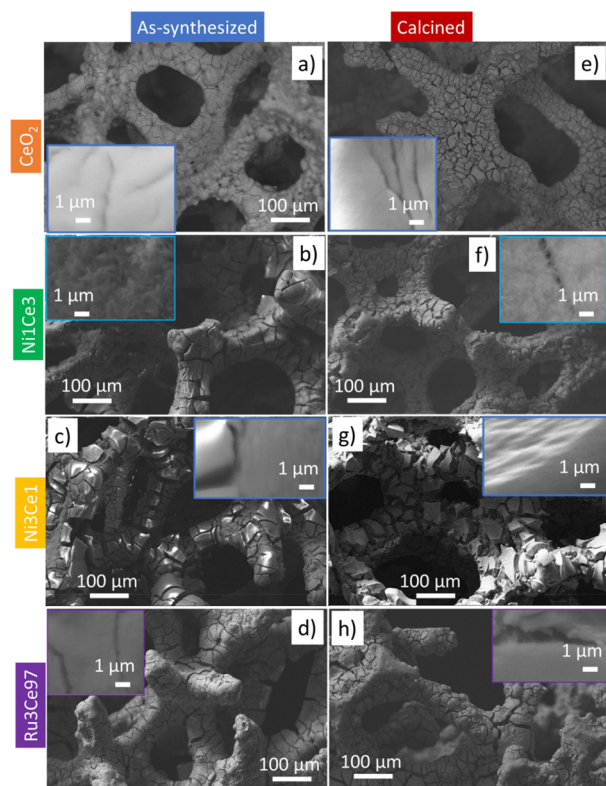


Figure 1. SEM images of as synthesized and calcined CeO_2 -based structured materials: CeO_2 (a, e); Ni_1Ce_3 (b, f); Ni_3Ce_1 (c, g); Ru_3Ce_97 (d, h).

sole CeO_2 sample is about 5–10 μm thick (Figure 1a), while 5–15 μm coatings are observed in the as-synthesized Ni- and Ru-containing samples (Figure 1b–d). In the latter, cracks develop due to both shearing stresses during drying and H_2 bubbles generated in the electrodeposition; remarkably the Ni_3Ce_1 catalyst contains a larger amount of cracks. High magnification images evidence the formation of nanoplatelets of CeO_2 randomly oriented, with a thin layer of more compact particles lying on it (the inset of Figure 1a). The average M/Ce values (M = Ni, Ru), estimated from EDS analyses, are very close to the nominal values in the electrolytic solution for all the samples as shown in Table 2.

XRD patterns of coated foams confirm the electrodeposition of nanocrystalline CeO_2 with a cubic fluorite structure (Figure 2a). Though some broad peaks in the Ni_3Ce_1 catalyst may be related to $\text{Ni}(\text{OH})_2$, the presence of Ni- and Ru-containing phases could not be proved by XRD. The nickel and ruthenium species are likely to simultaneously precipitate with the CeO_2 and be incorporated into its structure, or form well-dispersed hydroxides. Micro-Raman spectra in Figure 2b provides complementary information about the structure of the solids.^{44,45} The symmetrical stretching F_{2g} mode of CeO_2 , recorded in the spectra of sole CeO_2 at ca. 460 cm^{-1} , slightly

Table 2. Loading and Composition (Molar Ratio Obtained by EDS) of the CeO_2 and M– CeO_2 Coatings

catalyst	loading of coating (wt %)	Ni or Ru loading in the coating (wt %)	composition (atomic ratio)	
			M (Ni or Ru)/(M + Ce) molar ratio	Ce/(M + Ce) molar ratio
CeO_2	12.0 ± 0.7			
Ni_1Ce_3	14.7 ± 3.1	9.5	0.24 ± 0.09	0.76 ± 0.09
Ni_3Ce_1	15.1 ± 3.0	45.4	0.76 ± 0.02	0.24 ± 0.02
Ru_3Ce_97	18.6 ± 2.1	2.0	0.034 ± 0.01	0.966 ± 0.01

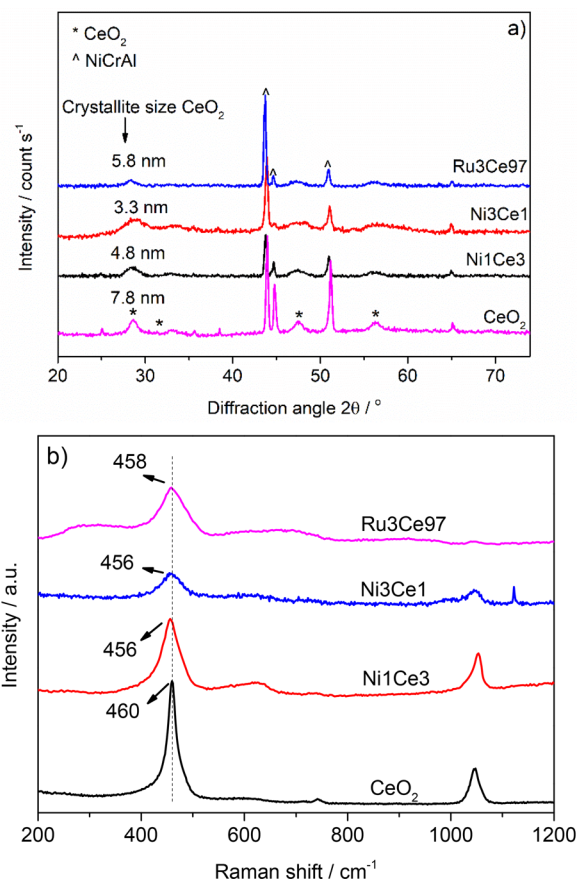


Figure 2. XRD patterns (a) and micro-Raman spectra (b) of as-synthesized structured materials.

moves toward lower Raman shift values in the presence of nickel and ruthenium, suggesting their incorporation into the CeO_2 lattice.^{46,47} Moreover, the asymmetry of the F_{2g} peak indicates the presence of oxygen vacancies or foreign ions. The presence of the defect-induced (D) mode band at around 600 cm^{-1} confirms the formation of oxygen defects in the CeO_2 structure, which could be also related to the partial substitution of Ce^{4+} by Ru^{4+} or Ni^{2+} in the fluorite framework.^{46,47} This band is more intense for the Ni_1Ce_3 sample and broader for Ru_3Ce_97 , a behavior that could be related to differences in the interaction between nickel and ruthenium with the CeO_2 . The peak at 1048 cm^{-1} is assigned to free nitrate ion from the electrolyte that remains in the solid after electrodeposition. While for the Ni_3Ce_1 sample a band at ca. 3650 cm^{-1} (not shown) is related to $\text{Ni}(\text{OH})_2$.⁴⁸

The calcination of the as-synthesized samples does not significantly modify the size and morphology of the particles in

the coating, though it causes an increase in the numbers of cracks (Figure 1e–h). The sintering of the CeO₂ structure is evidenced by XRD and Raman. In the diffraction patterns of calcined samples (Figure 3a), the CeO₂ reflections become

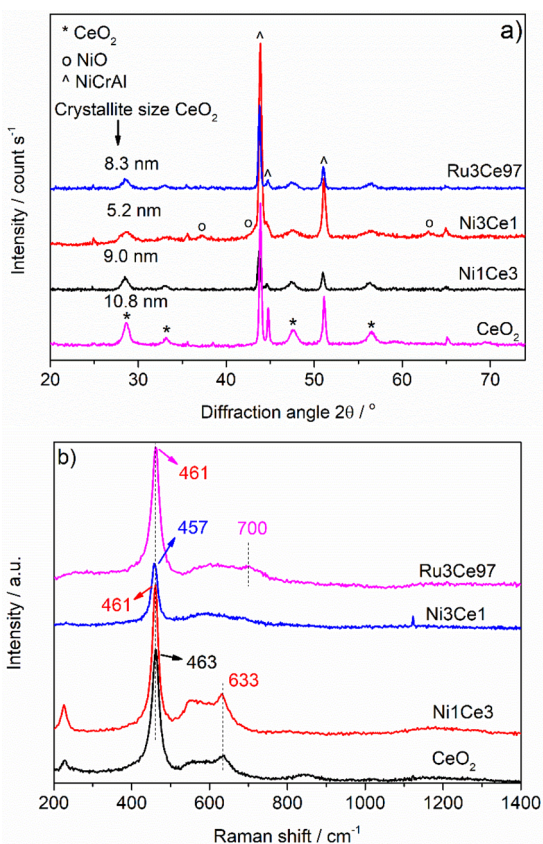


Figure 3. XRD patterns (a) and micro-Raman spectra (b) of calcined structured samples and CeO₂.

narrower and more intense than in the as-synthesized samples. Nevertheless, CeO₂ crystallite sizes in the catalysts are still in the nanometer range, i.e., 5–11 nm (Table 3). The presence of

Table 3. Crystallite Size of CeO₂ Calculated by the Scherrer Equation for As-Synthesized, Calcined, and Spent Structured Catalysts^a

	size at plane(111) 28.5 2θ (nm)		
	as synthesized	calcined	spent
Ni1Ce3	4.8	9.0	19.9
Ni3Ce1	3.3	5.2	12.6
Ru3Ce97	5.8	8.3	11.0
CeO ₂	7.8	10.8	

^aThe CeO₂ sample has been included for comparison purposes.

Ni or Ru seems to delay the sintering phenomena of the CeO₂ support. Only for the Ni3Ce1 sample is the segregated NiO phase detected. The absence of NiO and RuO₂ reflections in Ni1Ce3 and Ru3Ce97 patterns, respectively, could be related to a high dispersion of the oxides or to the inclusion of nickel and ruthenium into the CeO₂ structure. In the Raman spectra displayed in Figure 3b, the narrowing of the F_{2g} peak, due to the crystallite growth in the calcined samples, is accompanied by a shift toward higher Raman shift values. Hence, the

differences in the position of the peak for the metal-containing samples and the sole CeO₂ are reduced; the Ni3Ce1 sample displays the peak at the lower Raman shift value. The weak band at ca. 700 cm⁻¹ in Ru3Ce97 catalyst is related to the Ru–O–Ce interfacial bond, which has been attributed to a strong metal–support interaction;^{23,49} note that the expected band at ca. 970 cm⁻¹ is not detected. Remarkably, the spectra of CeO₂ and Ni1Ce3 structured samples show similar features, though the former spectrum is different than for precipitated CeO₂ (Figure S1). Bands at 225, 550, and 630 cm⁻¹ develop after calcination, but they are absent in the spectra of Ni3Ce1 catalyst. The peak at low Raman shift is related to the second-order transverse acoustic (2TA) mode of CeO₂ with lattice defects, generated by the incorporation of Ni²⁺ species into the CeO₂ structure.^{50,51} In these samples, the defect induced mode band is composed by the D₁ peak at ca. 600 cm⁻¹, due to oxygen vacancies, and the D₂ band at 630 cm⁻¹, due to cation substitution in the lattice.⁵² This D band is overlapped with the one-phonon LO (longitudinal optical) mode of defective nano NiO, located at 550 cm⁻¹; NiO also shows a broad band at 1100 cm⁻¹, attributed to a two-phonon 2LO mode.^{50,51} These characterization results indicate that NiO is incorporated into the CeO₂ lattice. The differences in the shape of the Ni3Ce1 spectrum could be related to the lower interaction between Ni and CeO₂. Actually, in this catalyst, XRD revealed that some NiO is segregated. The absence of NiO bands in the Raman spectra could be explained considering that the main peak of defective NiO at ca. 550 cm⁻¹, may be overlapped with the broad D band of the CeO₂, while the other vibrational modes are usually very weak and therefore not recorded.

The characterization of the coating surface in the calcined structured samples is performed by XPS (Figure 4). The Ce 3d core-level photoelectron spectra are complex and can be decomposed in several spin–orbit doublets denoted as v(n) and u(n). Three doublets are ascribed to the presence of Ce⁴⁺: v (~882 eV) and u (~901 eV)–Ce 3d⁹ 4f² O 2p⁴; v' (~886 eV) and u' (~907 eV)–Ce 3d⁹ 4f¹ O 2p⁵; v'' (~898 eV), u'' (~916 eV)–Ce 3d⁹ 4f⁰ O 2p⁶. Meanwhile two doublets: v₀ (~881 eV) and u₀ (~898 eV)–Ce 3d⁹ 4f² O 2p⁵; v' (~886 eV) and u' (~903 eV)–Ce 3d⁹ 4f¹ O 2p⁶ are assigned to Ce³⁺.^{53,54} The high energy parts of the Ce 3d_{5/2} spectra for samples Ni1Ce3 and Ni3Ce1 are overlapped with the low energy region of the Ni 2p_{1/2} spectra. This confers an additional complexity in the spectra analysis, and the component v₀ (~881 eV) of Ce³⁺ is difficult to be studied for these two samples. The reduction degree of cerium, expressed as Ce³⁺ percent, was calculated by taking into account these contributions as indicated by Zhang et al.,⁵⁵ and the results are indicated in Table 4. As expected, the reduction degree of Ce⁴⁺ is low, being the percentage of Ce³⁺ lower than 12% in all the studied samples. Figure 4 shows the deconvoluted Ce 3d, Ni 2p, and Ru 3p_{3/2} core-level spectra of the studied samples. In the case of the Ni 2p spectra (Figure 4b), the main peak of the Ni 2p_{3/2} signal for Ni1Ce3 appears at 854.8 eV, 1.0 eV shifted to the observed value for NiO (853.8 eV) and with the typical shakeup satellite of Ni²⁺ species. This shift to higher binding energy is due to the interaction between Ni species and CeO₂, in agreement with Raman spectra. The Ni 2p spectrum is similar for sample Ni3Ce1, but with higher relative intensity, and with the main peak appearing at a binding energy of 854.1 eV, nearer to that observed for NiO. This sample has a lower cerium content and the interaction between Ni and cerium species is weaker, as also suggested by

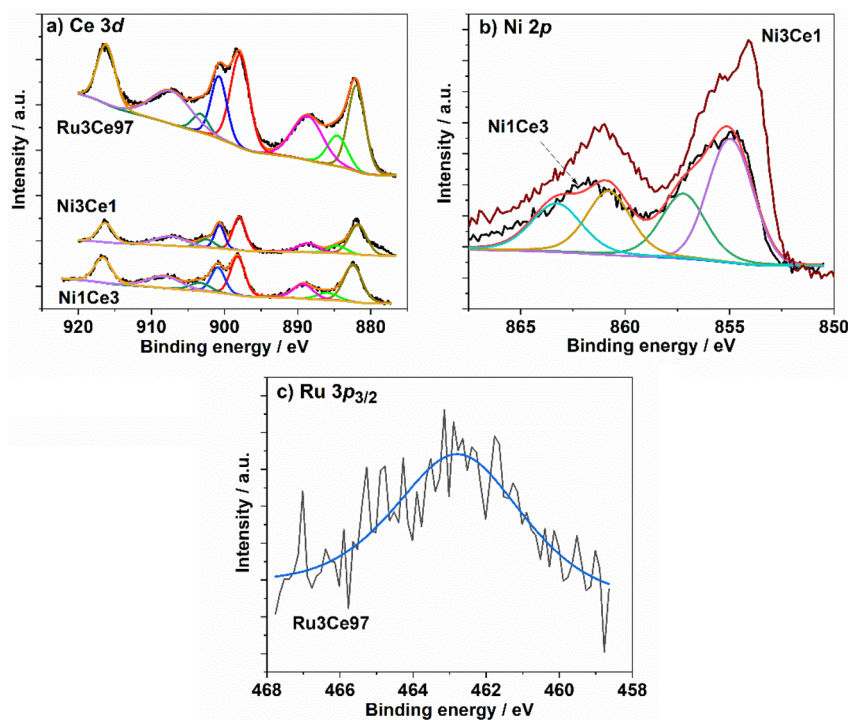


Figure 4. Ce 3d (a), Ni 2p (b), and Ru 3p_{3/2} (c) core-level spectra of the Ni1Ce3, Ni3Ce1, and Ru3Ce1 catalysts, respectively.

Table 4. Surface Chemical Composition (In Atomic Concentration, %) Determined by XPS

sample	C 1s	O 1s	Ni 2p _{3/2}	Ce 3d	Ru 3p _{3/2}	Ni/Ce	%Ce ³⁺
Ni1Ce3	29.49	51.25	13.71	5.51		2.49	10.4
Ni3Ce1	26.22	49.86	19.80	4.12		4.81	12.0
Ru3Ce97	34.36	51.07		14.04	0.63	0.045 ^a	10.0

^aRu/Ce atomic ratio.

Raman characterization. The Ru 3d signal is overlapped with the strong C 1s signal and its study not possible. For this reason, the Ru 3p_{3/2} signal was selected and shown in Figure 4c. This signal appears at 462.7 eV, very near to that observed for RuO₂ (462.5 eV). Therefore, it is possible to evidence the presence of Ru⁴⁺. The O 1s core-level spectra show two contributions in all the studied samples: 529.7 eV (73%) and 531.5 eV (27%) for sample Ni1Ce3, 529.5 eV (77%) and 531.3 eV (23%) for sample Ni3Ce1, and 529.0 eV (85%) and 531.4 eV (15%) for sample Ru3Ce97. The main peak is mainly associated with lattice oxygen of NiO for samples Ni1Ce3 and Ni3Ce1, and lattice oxygen for CeO₂ in sample Ru3Ce97. The shoulder at higher binding energy is assigned to hydroxyl groups. The C 1s core level signals (not shown) of the samples Ni1Ce3 and Ru3Ce97, with a higher Ce content, show a contribution at about 289.0 eV due to the presence of surface cerium carbonate, typical of cerium containing compounds. This contribution at high binding energy was not observed in the case of the sample with a low Ce content (Ni3Ce1).

Table 4 shows the surface atomic concentration for the studied samples. It is relevant the high percentage of C, and the high relative surface Ni content, since the observed Ni/Ce atomic ratios are much higher than the nominal values and those observed by EDS. 2.49 for sample Ni1Ce3 (nominal Ni/Ce = 0.33) and 4.81 for sample Ni3Ce1 (nominal Ni/Ce = 3). In the case of sample Ru3Ce97, the observed Ru/Ce atomic ratio (0.045) is higher than the nominal one (0.031). This indicates that CeO₂ has some promotion effect on Ni and Ru.

The H₂-TPR profiles of the coated foams after calcination are shown in Figure 5. The H₂ consumption for the sole CeO₂

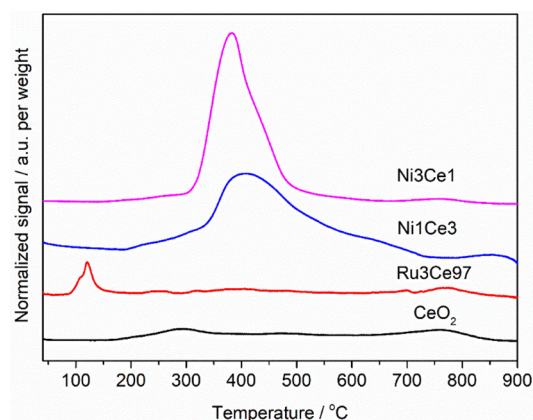


Figure 5. H₂-TPR profiles of CeO₂-, Ru3Ce97-, Ni1Ce3-, and Ni3Ce1-structured calcined samples.

sample occurs in three steps, related to the reduction of surface (approximate 300 and 480 °C) and bulk CeO₂ (760 °C).^{56,57} The contribution of Ni from the foam support could be not ruled out. In the Ru-containing catalyst, the two overlapped peaks at ca. 106 and 120 °C could be related to RuO₂ species highly and weakly interacting with CeO₂, as previously reported for impregnated catalysts.²³ However, in the bulk

catalyst here investigated, the embedment of the species in the structure could also delay the reduction.²² The weak peaks above 200 °C in the profile of Ru3Ce97 could be associated with the reduction of surface CeO₂, fostered by the presence of ruthenium since the Ce–O bond is weakened.⁴⁹ While the reduction of bulk CeO₂ is observed as a weak peak at ca. 770 °C. In the Ni1Ce3 and Ni3Ce1 catalysts, an asymmetric peak is recorded in the 200–700 °C temperature range. It is ascribed to the overlapped reduction of adsorbed oxygen (shoulder between 200 and 300 °C), NiO dispersed (main peak around 370 °C), NiO highly interacting with the CeO₂ support (shoulder around 450 °C), and the reduction of CeO₂ surface oxygen, this latter is shifted to a lower temperature than in the sole CeO₂ due to the substitution of Ni.^{18,37} More precisely, the adsorbed oxygen has been reported to be on CeO₂ vacancies, which are generated in the NiO–CeO₂ solid solution.⁵⁸ For the Ni1Ce3 catalyst, the shift of the reduction profile toward higher temperatures in comparison to the one of Ni3Ce1, and the increase in the intensity of the shoulder at approximately 600 °C confirm the enhanced interaction between NiO and CeO₂ for this catalyst, above evidenced by Raman and XPS analyses.

3.2. Catalytic Tests and Characterization of Spent Structured Catalysts. The coating composition largely determines both the CO₂ conversion and CH₄ selectivity (Figure 6). Ru3Ce97 catalyst is poorly active in the methanation; for instance, at 400 °C a 20% CO₂ conversion is achieved, and more remarkably, in the 300–450 °C range, the selectivity to CH₄ is only 40–46%. The increase in the activity above 450 °C could be related to the contribution of

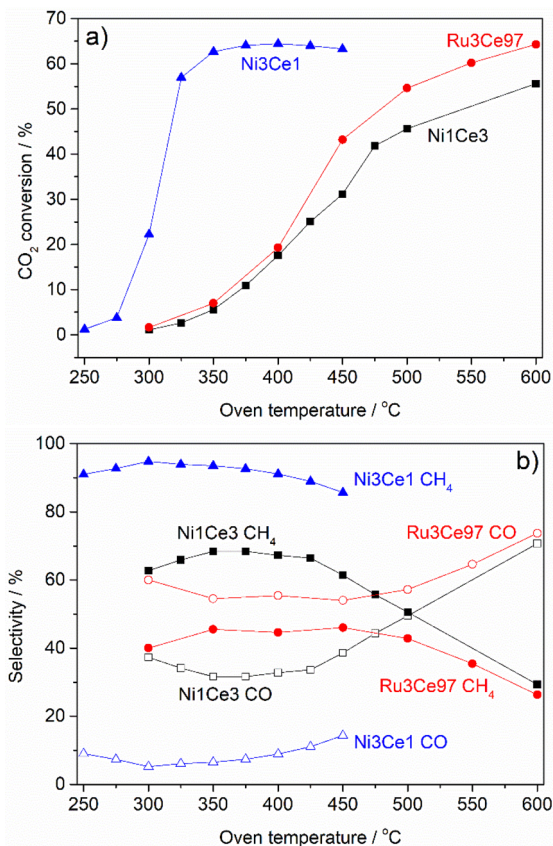


Figure 6. CO₂ conversion (a) and CH₄ and CO selectivity (b) over Ru3Ce97-, Ni1Ce3-, and Ni3Ce1-structured catalysts.

the RWGS since the CO production also largely increases. The low ability of the catalyst to convert CO₂ to CH₄, more exothermic than the CO₂ to CO reaction may explain, the rather flat temperature profiles measured along the center of the catalytic bed (Figure S2a), even when the CO₂ conversion reaches a 40–50% value.

SEM images of the spent Ru3Ce97 catalyst in Figure S3c show that the solid is well-adhered to the metallic foam after catalytic tests. However, the sintering of the CeO₂ structure, already observed after calcination, seems to continue after reduction pretreatment and catalytic tests; i.e., the CeO₂ crystallite size is doubled in the spent catalyst in comparison to the calcined material (Figure S4a and Table 3). Elemental mapping of the foam surface by EDS evidence that Ru and Ce are well distributed in the coating (Figure S5a–d). HRTEM images show that this coating is actually made by nano-CeO₂ particles showing well-defined lattice fringes with *d*-spacings of 0.312 and 0.271 nm due to (111) and (200) fluorite-type CeO₂ structure (Figure 7a). Ru amorphous particles, in the 5

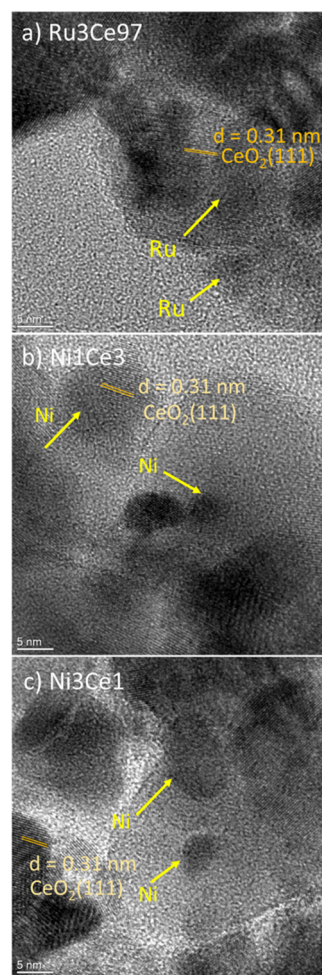


Figure 7. HRTEM images of the spent structured catalysts (a) Ru3Ce97, (b) Ni1Ce3, and (c) Ni3Ce1.

to 10 nm size range, are embedded in and highly interacting with the CeO₂ (Figure 7a). The reduction of RuO₂ to Ru⁰ could be assumed by the disappearance of the 700 cm⁻¹ peak in the Raman spectra (Figure S6).

Hence, the low methane production of the Ru-containing catalyst could be related to the embedment of Ru into the

CeO₂ structure and the unbalance between CO₂ activation in the oxygen vacancies or Ru and H₂ dissociation in the Ru metallic sites.^{20,23} This latter behavior could be more remarkable at the high space velocity value used in this work in comparison to the values reported in the literature, 320,000 mL g_{cat}⁻¹ h⁻¹ (H₂/CO₂/N₂ = 4/1/1 v/v) vs 72,000 mL g_{cat}⁻¹ h⁻¹ (H₂/CO₂/N₂ = 4/1/5 v/v),³⁵ 150,000 mL g_{cat}⁻¹ h⁻¹ (H₂/CO₂/Ar = 3.2/1/40 v/v),²⁰ and 4800 mL g_{cat}⁻¹ h⁻¹ (CO₂/H₂/He = 1/4/15 v/v).²³ Indeed in a test with an impregnated pelletized catalyst (Figure S7), CO₂ and CH₄ selectivity values increased, the latter being around 80%, but they are still far from the ones reported in the literature. Another interesting case to compare with our data has been recently reported by Cimino and co-workers;¹³ in that work, Ru is both directly electrodeposited on a Ni foam and impregnated on a CeO₂-coated Ni foam. Note that in our Ru3Ce97 foam catalyst, Ru and CeO₂ are simultaneously deposited on the NiCrAl foam. Detailed information on the comparison is summarized in Table S1. Although substantial differences in Ru loading and reaction conditions (the composition of the feedstock and GHSV) make it difficult to directly compare the results in both works, some highlights on the selectivity of CH₄ can be discussed. The selectivity in CH₄ of our Ru3Ce97 catalyst is 40–46%, in between the values obtained over the catalysts with Ru directly deposited on the Ni foam (10%) and Ru deposited on a CeO₂-coated Ni foam (98%). This suggests that not only the presence of CeO₂ support plays a role on the CO₂ methanation, but also the way Ru is incorporated into the CeO₂ support may modify the activity. Ru-embedded in CeO₂, obtained by the electrodeposition route (in our case), exhibits a higher reaction rate of CO₂ conversion but lower selectivity in CH₄ than Ru-impregnated CeO₂,¹³ suggesting a lower rate for H₂ dissociation and, consequently, an unbalance between CO₂ and H₂ activation, though this needs a further study to compare both types of catalysts under similar reaction conditions.

The Ni1Ce3 catalyst behaves like the Ru3Ce97 sample, though it is slightly more selective to CH₄, 61–68%, and shows a lower CO₂ conversion above 400 °C, suggesting a poorer RWGS activity. The higher Ni loading in the Ni3Ce1 catalyst not only improves the CO₂ conversion at low temperature (e.g., at 325 °C a CO₂ conversion of 57% is reached) but also the CH₄ selectivity (Figure 6). Throughout all the temperatures investigated, CH₄ is the main reaction product, with selectivities in the 86–95% range, resulting in productivity of CH₄ of 24.7, 62.7, and 68.7 L_{CH4} g_{cat}⁻¹ h⁻¹ at 300, 325, and 350 °C, respectively. A plot of CO₂ conversion versus the outlet temperature of the catalytic bed shows that the CO₂ conversion of the Ni3Ce1 is still far from the equilibrium conversion value of CO₂ at a temperature of approximately 500 °C (Figure S8). Hence, the comparisons between catalysts are performed in reaction conditions not governed by the thermodynamic equilibrium. Similar CO₂ conversion and CH₄ selectivity values are obtained over another set of Ni3Ce1 foams confirming the reproducibility of the electrodeposition coating method for the catalyst preparation (Figure S9). The temperature measured within the catalytic bed is characteristic of an exothermic reaction, with the hotspot positions at 1–2 mm near the outlet of the bed, probably due to the high space velocity values. The temperature inside the bed for Ni3Ce1, shown in Figure S2c, is almost similar to the oven temperature at 250 and 275 °C when the CO₂ conversion is negligible. While the temperature increment is about 82–85

°C higher when the CO₂ conversion is 56–64% and the CH₄ selectivity 93–94%, at oven temperatures of 325–375 °C. However, the temperature increment decreases significantly, e.g., to 69–56 °C, with a further increase in the oven temperature from 400 to 450 °C, although the CO₂ conversion only decreases by about 1.5%. This is explained by the contribution of the endothermic RWGS reaction, also associated with an increase in CO selectivity from 8.8 to 14.3%. The Ni3Ce1 catalyst is less active than NiAl and NiCeAl structured catalysts based on hydrothermalite-type compounds also prepared by electrodeposition.¹²

After methanation, the coating is partially detached in some exposed areas; however, it is worthy to note that the catalytic film in the less active Ni1Ce3 sample is more stable than in Ni3Ce1 (Figure S3a,b). In the diffraction patterns of the spent catalysts shown in Figure S4a, the reflections attributed to Ni⁰ in the catalytic coating cannot be distinguished from those of the NiCrAl support. The absence of both NiO reflections in the diffraction pattern of Ni3Ce1 and the bands due to Ni²⁺ incorporation into CeO₂ in the Raman spectra of Ni1Ce3 (Figure S10), which were present in the calcined samples, suggest that that nickel species are reduced after the prereduction treatment and catalytic tests. The XPS study of the spent Ni1Ce3 and Ni3Ce1 foam catalysts also confirms the presence of Ni⁰. Their Ni 2p_{3/2} core level spectra are shown in Figure S11. Both spectra show two contributions at 852.9 and 855.5–855.7 eV. The former, more intense in the case of the spent Ni3Ce1, is assigned to the presence to Ni⁰, and the latter to Ni²⁺. The presence of Ni²⁺ can be derived from the surface air oxidation of Ni⁰, though some highly interacting Ni species not easily reduced could not be discarded. In the case of the Ce 3d core level spectra of these spent catalysts (Figure S11), a reduction of Ce⁴⁺ to Ce³⁺ is also observed in both cases. Like for the Ru3Ce97 catalyst, the CeO₂ structure sinters during tests, Figure S4a, but the defect induced mode band at ca. 633 cm⁻¹ is still observed for Ni1Ce3 (Figure S10). Note that a higher Ni loading delays the CeO₂ crystallite growth (Figure S4a). In the coatings of the spent catalysts, Ni and Ce distributions are well correlated, as observed in EDS elemental maps (Figure S5e–h). While HRTEM images do not evidence remarkable differences in the morphology of the catalysts depending on the Ni loading. Both types of spent catalysts contain nanocrystalline CeO₂ (with *d*-spacing of approximately 0.31 nm for the (111) plane), similar to that present in the Ru3Ce97 coating, and amorphous Ni nanoparticles with sizes around 5–20 nm (Figure 7a,b).

Hence, the differences in activity observed for Ni1Ce3 and Ni3Ce1 seem not to be related to the Ni particle size but to its amount. The low activity and selectivity in CH₄ over the low loaded Ni1Ce3 catalyst are likely related to a decrease in the H₂ dissociation activity, though the effect of the lower reducibility could not be discarded. The larger Ni–CeO₂ interface and vacancies for Ni1Ce3 than for Ni3Ce1 seem to be not enough to achieve a higher performance. The role of the Ni loading could be also more evident due to the high space value in the tests, 320,000 mL g_{coating}⁻¹ h⁻¹, which may suppress the CO to CH₄ step. The Ni1Ce3 sample behaves like catalysts with similar Ni loadings reported by Cárdenas-Arenas et al.²⁸ and a 20% Ni–CeO₂ catalyst prepared by the colloidal solid combustion.³⁰ Conversely, over NiO–CeO₂ mixed oxides prepared by the template method, a low CO₂ conversion but high CH₄ selectivity are achieved.⁵⁰ Furthermore, for the electrodeposited catalysts here investigated, the

in situ formation of the solid may also lead to differences in the catalyst properties. To shed light on the role of the properties of the electrodeposited coating on the activity, Ni1Ce3, and Ni3Ce1 powder catalysts were prepared by conventional coprecipitation and calcination.

3.3. Pelletized vs Structured NiCe Catalysts. The coprecipitated catalysts contain similar crystalline phases than the electrodeposited ones (Figure 8a). Moreover, the Ni–

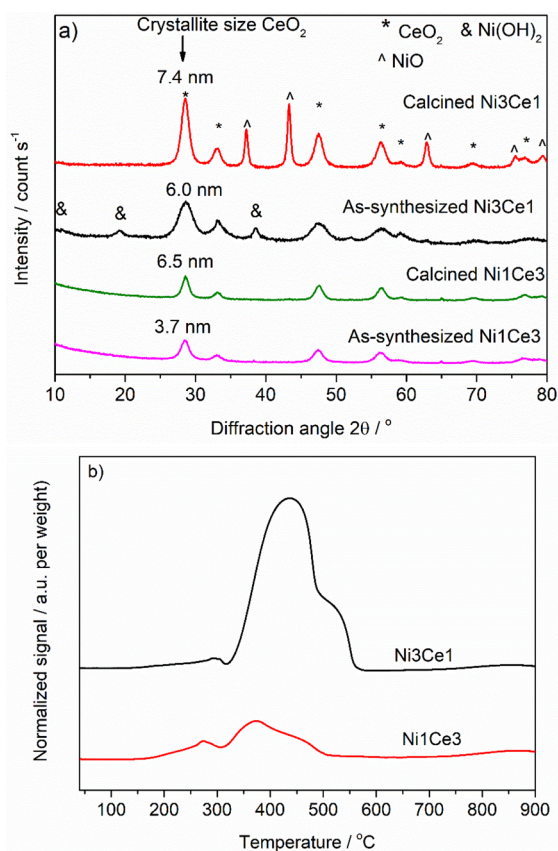


Figure 8. Characterization of pelletized catalysts: (a) XRD patterns of as-synthesized and calcined samples and (b) H₂-TPR profiles of calcined samples.

CeO₂ interaction, observed in the Ni1Ce3 foam, is also established in coprecipitated catalysts for the low loaded Ni catalyst, e.g., oxygen vacancies generated by the inclusion of Ni²⁺ into the CeO₂ are observed in the Raman spectra (not shown). The differences in the position and intensity of the H₂-TPR peaks for coprecipitated and electrodeposited samples suggest some differences in the type and amount of nickel species (Figure 8b). In particular, the Ni1Ce3 catalyst is reduced at higher temperatures in the structured form than in the pellets, while the behavior is reversed for the high loaded samples. The XPS study of these samples also shows differences. The Ni 2p_{3/2} core level spectra of calcined Ni1Ce3 and Ni3Ce1 catalysts (Figure S12) show a broad main Ni 2p_{3/2} main peak as a result of different Ni²⁺ species. In both cases, and mainly in sample Ni3Ce1, the maximum of the main Ni 2p_{3/2} peak appears shifted to high binding energy (855.7 eV). This shift was also observed in foam samples and it was attributed to the interaction between Ni²⁺ species and CeO₂. In the case of the Ce 3d spectra, significant reduction of

Ce⁴⁺ to Ce³⁺ was observed in both pelletized catalysts but more pronounced in the case of the Ni3Ce1 catalyst.

The catalytic results obtained over pelletized catalysts are displayed in Figure 9. They clearly show that, like for the

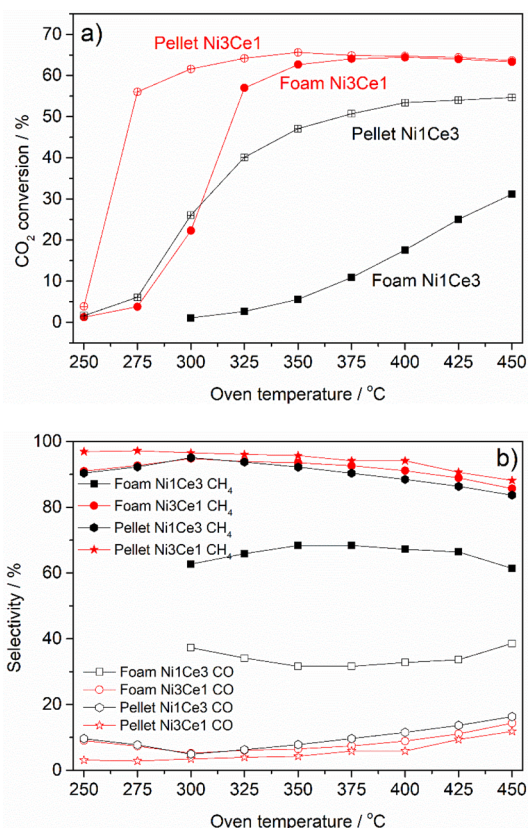


Figure 9. Comparison of the performance of pelletized and foam Ni1Ce3 and Ni3Ce1: (a) CO₂ conversion and (b) CH₄ and CO selectivity.

foams, the Ni loading determines the activity. In the low-temperature region (275–300 °C), the CO₂ conversion is around 56% for Ni3Ce1 and negligible for Ni1Ce3. Remarkably, pelletized catalysts overcome structured ones, not only in terms of conversion but more importantly in the selective production of CH₄. The Ni1Ce3 pelletized catalyst achieves a 92% CH₄ selectivity even at very low values of CO₂ conversions. The pelletized Ni3Ce1 catalyst shows good activity in the selective conversion of CO₂ to CH₄ at 275 °C, close to that achieved for a pelletized NiCeAl catalyst,⁵⁹ though at different space velocities 320,000 and 480,000 mL g⁻¹ h⁻¹, respectively. The Ni3Ce1 pellet catalyst exhibits similar CO₂ conversion and CH₄ selectivity at a temperature higher than 350 °C than the Ni3Ce1 foam, and it has a productivity of CH₄ approximately 75.3 L_{CH₄} g_{cat}⁻¹ h⁻¹ at 350 °C. Note that the plot of the conversion versus the outlet temperature shows that the conversions of CO₂ on both pelletized and structured catalysts of Ni1Ce3 and Ni3Ce1 are far from thermodynamic limitation (Figure S13).

The Arrhenius plots and apparent activation energies obtained for CO₂ conversions below 25% for all the structured and pelletized catalysts (except for Ni3Ce1 pellets) are plotted in Figure 10. The temperature ranges used for these plots are 250–300 °C for Ni3Ce1-Foam and Ni1Ce3-Pellet, and 300–400 °C for Ru3Ce97-Foam and Ni1Ce3-Foam. Note that the

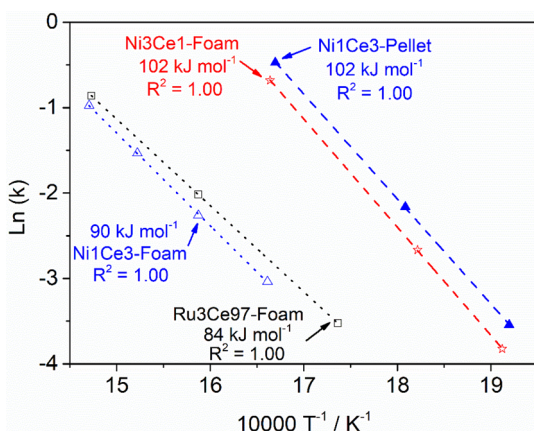


Figure 10. Arrhenius plot for different catalysts. The slope of the fitted linear regression is given by $-E_a/R$. The conversion at each temperature point was lower than 25% to ensure that the selected temperature was in the kinetic range.

reaction on the catalysts is far from the thermodynamic equilibrium within these temperature ranges (Figure 6a and Figure 9a). A linear fit with a great correlation was found for all four catalysts ($R^2 \geq 0.999$). The apparent activation energies are calculated to be approximately 84 kJ mol^{-1} for Ru3Ce97-Foam, 90 kJ mol^{-1} for Ni1Ce3-Foam, and 102 kJ mol^{-1} for both Ni1Ce3-Pellet and Ni3Ce1-Foam. These values of the activation energies are similar to those previously reported in the literature, e.g., 86.7 kJ mol^{-1} for 5 wt % Ru/CeO₂ catalyst⁶⁰ or 85.8 kJ mol^{-1} for Ru/Ni (direct electrodeposition on Ni foam) and 87.5 kJ mol^{-1} for Ru-impregnated on CeO₂-coated Ni foam,¹³ and in a range of $95\text{--}107 \text{ kJ mol}^{-1}$ for Ni/CeO₂ catalysts.⁶¹ Note that the apparent activation energy values depend on both the type of catalysts and the operating conditions (e.g., reactant composition, reduction temperature, and treatment conditions).^{61,62} Therefore, it is challenging to have a fair comparison with the results from the literature. However, the close values of E_a for each pair of Ru3Ce97-Foam and Ni1Ce3-Foam or Ni3Ce1-Foam and Ni1Ce3-Pellet suggest that each pair of catalysts may follow a similar reaction pathway.

The pellet Ni1Ce3 catalyst (Figure S14a) shows higher hotspot temperatures than those of the foam Ni1Ce3 catalyst (Figure S14b) due to both higher CO₂ conversion and CH₄ selectivity (or lower CO selectivity) of the pellet than the foam. However, the higher heat transfer over the foam catalyst could also modify the temperature profile, and since the temperature is not only a cause but also a consequence of the reaction, an accurate comparison of the activity of both types of catalysts is tricky. Some more work is in progress to further shed light on the differences between co-precipitated and electrodeposited materials.

4. CONCLUSIONS

CeO₂-based structured catalysts for the CO₂ methanation, containing either Ni with different loadings or Ru, are easily prepared through a direct coating process, the electrodeposition, and the subsequent calcination step. CeO₂ coatings with well-dispersed Ru and Ni species or segregated NiO (for high Ni loadings) deposit on the surface of NiCrAl foams of high pore density; the quality of the coating decreases as the Ni content increases. Under harsh reaction conditions (high space velocity and CO₂ concentration in the feedstock) the activity

and selectivity of the catalysts significantly depend on both metal loading and the preparation method. The low Ni loaded structured catalyst (9.5 wt % Ni in the coating) shows a poor activity, e.g., 6% conversion of CO₂ and 68% selectivity of CH₄ at 350 °C, which is significantly lower than the activity of a pelletized counterpart at the same oven temperature (47% conversion of CO₂ and 92% selectivity of CH₄). Strong metal–support interaction and the unbalance between H₂ dissociation and CO₂ activation sites in the structured catalyst may explain this behavior. With high Ni content (approximately 45 wt %), both structured and pelletized Ni3Ce1 catalysts exhibit rather similar CH₄ productivity at 350 °C, e.g., 68.7 and 75.3 L_{CH₄} g_{Ni}⁻¹ h⁻¹, respectively. Though the latter is more active at lower temperatures. In contrast, the low activity of both Ru–CeO₂ structured (with a strong Ru–CeO₂ interaction) and pelletized impregnated catalysts in comparison to the results reported in the literature suggests that the reaction conditions significantly determine their activity for CO₂ methanation.

■ ASSOCIATED CONTENT

Supporting Information

The Supporting Information is available free of charge at <https://pubs.acs.org/doi/10.1021/acs.iecr.0c06024>.

Raman spectra of CeO₂ prepared by precipitation and electrodeposition; temperature profiles recorded on different foam catalysts; SEM/EDS images of spent foam catalysts; XRD patterns of spent catalysts; SEM images and elemental mappings of spent structured catalysts; Raman spectra of Ru3Ce97 spent structured catalyst; comparison of the CO₂ methanation activity of the pellet and foam Ru3Ce97 catalysts; CO₂ conversion versus outlet temperature over different foam catalysts; reproducibility check for Ni3Ce1 foam catalysts in terms of CO₂ conversion and CH₄ selectivity; Raman spectra of spent Ni1Ce3 foam catalyst; XPS measurements for Ni-based foam catalysts (the spent) and pellet catalysts (the calcined samples); CO₂ conversion versus outlet temperature over Ni-based pellet and foam catalysts; temperature profiles recorded on Ni1Ce3 pellet and Ni3Ce1 foam catalyst; comparison of the activity of Ru3Ce97 catalyst with the results from the literature (PDF)

■ AUTHOR INFORMATION

Corresponding Author

Patricia Benito – Dipartimento di Chimica Industriale “Toso Montanari”, University of Bologna, 40136 Bologna, Italy; orcid.org/0000-0003-0487-6782; Email: patricia.benito3@unibo.it

Authors

Phuoc Hoang Ho – Dipartimento di Chimica Industriale “Toso Montanari”, University of Bologna, 40136 Bologna, Italy; orcid.org/0000-0001-8571-4114

Giancosimo Sanghez de Luna – Dipartimento di Chimica Industriale “Toso Montanari”, University of Bologna, 40136 Bologna, Italy

Arturo Poggi – Dipartimento di Chimica Industriale “Toso Montanari”, University of Bologna, 40136 Bologna, Italy

Monica Nota – Dipartimento di Chimica Industriale “Toso Montanari”, University of Bologna, 40136 Bologna, Italy

Enrique Rodríguez-Castellón – Universidad de Málaga, Departamento de Química Inorgánica, Facultad de Ciencias, 29071 Málaga, Spain; orcid.org/0000-0003-4751-1767

Giuseppe Fornasari – Dipartimento di Chimica Industriale “Toso Montanari”, University of Bologna, 40136 Bologna, Italy

Angelo Vaccari – Dipartimento di Chimica Industriale “Toso Montanari”, University of Bologna, 40136 Bologna, Italy

Complete contact information is available at:
<https://pubs.acs.org/10.1021/acs.iecr.0c06024>

Author Contributions

^{||}P.H.H. and G.S.d.L. contributed equally.

Notes

The authors declare no competing financial interest.

ACKNOWLEDGMENTS

We thank Alantum for supplying metal foams. E.R.C. thanks the Ministerio de Ciencia, Innovación y Universidades (project RTI2018-099668-BC22), the Junta de Andalucía (project UMA18-FEDERJA-126), and the FEDER funds for financial support.

REFERENCES

- (1) Thema, M.; Bauer, F.; Sterner, M. Power-to-Gas: Electrolysis and methanation status review. *Renewable Sustainable Energy Rev.* **2019**, *112*, 775–787.
- (2) Wulf, C.; Zapp, P.; Schreiber, A. Review of Power-to-X Demonstration Projects in Europe. *Front. Energy Res.* **2020**, *8*, 191.
- (3) Lee, W. J.; Li, C.; Prajitno, H.; Yoo, J.; Patel, J.; Yang, Y.; Lim, S. Recent trend in thermal catalytic low temperature CO₂ methanation: A critical review. *Catal. Today* **2020**, DOI: [10.1016/j.cattod.2020.02.017](https://doi.org/10.1016/j.cattod.2020.02.017).
- (4) Schollenberger, D.; Bajohr, S.; Gruber, M.; Reimert, R.; Kolb, T. Scale-up of innovative honeycomb reactors for power-to-gas applications – The project Store&Go. *Chem. Ing. Tech.* **2018**, *90*, 696–702.
- (5) Danaci, S.; Protasova, L.; Lefevre, J.; Bedel, L.; Guilet, R.; Marty, P. Efficient CO₂ methanation over Ni/Al₂O₃ coated structured catalysts. *Catal. Today* **2016**, *273*, 234–243.
- (6) Frey, M.; Bengaouer, A.; Geffraye, G.; Edouard, D.; Roger, A.-C. Aluminum open cell foams as efficient supports for carbon dioxide methanation catalysts: pilot-scale reaction results. *Energy Technol.* **2017**, *5*, 2078–2085.
- (7) Li, Y.; Zhang, Q.; Chai, R.; Zhao, G.; Liu, Y.; Lu, Y.; Cao, F. Ni-Al₂O₃/Ni-foam catalyst with enhanced heat transfer for hydrogenation of CO₂ to methane. *AIChE J.* **2015**, *61*, 4323–4331.
- (8) Fukuhara, C.; Hayakawa, K.; Suzuki, Y.; Kawasaki, W.; Watanabe, R. A novel nickel-based structured catalyst for CO₂ methanation: A honeycomb-type Ni/CeO₂ catalyst to transform greenhouse gas into useful resources. *Appl. Catal., A* **2017**, *532*, 12–18.
- (9) Ratchahat, S.; Sudoh, M.; Suzuki, Y.; Kawasaki, W.; Watanabe, R.; Fukuhara, C. Development of a powerful CO₂ methanation process using a structured Ni/CeO₂ catalyst. *J. CO₂ Util.* **2018**, *24*, 210–219.
- (10) Neuberg, S.; Pennemann, H.; Shanmugam, V.; Thiermann, R.; Zapf, R.; Gac, W.; Greluk, M.; Zawadzki, W.; Kolb, G. CO₂ Methanation in Microstructured Reactors – Catalyst Development and Process Design. *Chem. Eng. Technol.* **2019**, *42*, 2076–2084.
- (11) Navarro, J. C.; Centeno, M. A.; Laguna, O. H.; Odriozola, J. A. Ru-Ni/MgAl₂O₄ structured catalyst for CO₂ methanation. *Renewable Energy* **2020**, *161*, 120–132.
- (12) Ho, P. H.; Sanghez de Luna, G.; Ospitali, F.; Fornasari, G.; Vaccari, A.; Benito, P. Open-cell foams coated by Ni/X/Al

hydrocalcite-type derived catalysts (X = Ce, La, Y) for CO₂ methanation. *J. CO₂ Utiliz.* **2020**, *42*, 101327.

(13) Cimino, S.; Cepollaro, E. M.; Lisi, L.; Fasolin, S.; Musiani, M.; Vázquez-Gómez, L. Ru/Ce/Ni Metal Foams as Structured Catalysts for the Methanation of CO₂. *Catalysts* **2021**, *11*, 13.

(14) Gac, W.; Zawadzki, W.; Rotko, M.; Greluk, M.; Slowik, G.; Kolb, G. Effects of support composition on the performance of nickel catalysts in CO₂ methanation reaction. *Catal. Today* **2020**, *357*, 468–482.

(15) Cárdenas-Arenas, A.; Quindimil, A.; Davó-Quiñonero, A.; Bailón-García, E.; Lozano-Castelló, D.; De-La-Torre, U.; Pereda-Ayo, B.; González-Marcos, J. A.; González-Velasco, J. R.; Bueno-López, A. Isotopic and in situ DRIFTS study of the CO₂ methanation mechanism using Ni/CeO₂ and Ni/Al₂O₃ catalysts. *Appl. Catal., B* **2020**, *265*, 118538.

(16) Jomjaree, T.; Sintuya, P.; Srifa, A.; Koo-amornpattana, W.; Kiatphuengporn, S.; Assabumrungrat, S.; Sudoh, M.; Watanabe, R.; Fukuhara, C.; Ratchahat, S. Catalytic performance of Ni catalysts supported on CeO₂ with different morphologies for low-temperature CO₂ methanation. *Catal. Today* **2020**, DOI: [10.1016/j.cattod.2020.08.010](https://doi.org/10.1016/j.cattod.2020.08.010).

(17) Muroyama, H.; Tsuda, Y.; Asakoshi, T.; Masitah, H.; Okanishi, T.; Matsui, T.; Eguchi, K. Carbon dioxide methanation over Ni catalysts supported on various metal oxides. *J. Catal.* **2016**, *343*, 178–184.

(18) Le, T. A.; Kim, M. S.; Lee, S. H.; Kim, T. W.; Park, E. D. CO and CO₂ methanation over supported Ni catalysts. *Catal. Today* **2017**, *293–294*, 89–96.

(19) Wang, F.; He, S.; Chen, H.; Wang, B.; Zheng, L.; Wei, M.; Evans, D. G.; Duan, X. Active Site Dependent Reaction Mechanism over Ru/CeO₂ Catalyst toward CO₂ Methanation. *J. Am. Chem. Soc.* **2016**, *138*, 6298–6305.

(20) Dreyer, J. A. H.; Li, P.; Zhang, L.; Beh, G. K.; Zhang, R.; Sit, P. H.-L.; Teoh, W. Y. Influence of the oxide support reducibility on the CO₂ methanation over Ru-based catalysts. *Appl. Catal., B* **2017**, *219*, 715–726.

(21) Boaro, M.; Colussi, S.; Trovarelli, A. Ceria-Based Materials in Hydrogenation and Reforming Reactions for CO₂ Valorization. *Front. Chem.* **2019**, *7*, 28.

(22) Sharma, S.; Sravan Kumar, K. B.; Chandnani, Y. M.; Phani Kumar, V. S.; Gangwar, B. P.; Singhal, A.; Deshpande, P. A. Mechanistic insights into CO₂ methanation over Ru-Substituted CeO₂. *J. Phys. Chem. C* **2016**, *120*, 14101–14112.

(23) Guo, Y.; Mei, S.; Yuan, K.; Wang, D.-J.; Liu, H.-C.; Yan, C.-H.; Zhang, Y.-W. Low-Temperature CO₂ Methanation over CeO₂-Supported Ru Single Atoms, Nanoclusters, and Nanoparticles Competitively Tuned by Strong Metal–Support Interactions and H-Spillover Effect. *ACS Catal.* **2018**, *8*, 6203–6215.

(24) Li, M.; Amari, H.; van Veen, A. C. Metal-oxide interaction enhanced CO₂ activation in methanation over ceria supported nickel nanocrystallites. *Appl. Catal., B* **2018**, *239*, 27–35.

(25) Winter, L. R.; Gomez, E.; Yan, B.; Yao, S.; Chen, J. G. Tuning Ni-catalyzed CO₂ hydrogenation selectivity via Ni-ceria support interactions and Ni-Fe bimetallic formation. *Appl. Catal., B* **2018**, *224*, 442–450.

(26) Aitbekova, A.; Wu, L.; Wrasman, C. J.; Boubnov, A.; Hoffman, A. S.; Goodman, E. D.; Bare, S. R.; Cargnello, M. Low-Temperature Restructuring of CeO₂-Supported Ru Nanoparticles Determines Selectivity in CO₂ Catalytic Reduction. *J. Am. Chem. Soc.* **2018**, *140*, 13736–13745.

(27) Cárdenas-Arenas, A.; Quindimil, A.; Davó-Quiñonero, A.; Bailón-García, E.; Lozano-Castelló, D.; De-La-Torre, U.; Pereda-Ayo, B.; González-Marcos, J. A.; González-Velasco, J. R.; Bueno-López, A. Design of active sites in Ni/CeO₂ catalysts for the methanation of CO₂: tailoring the Ni-CeO₂ contact. *Appl. Mater. Today* **2020**, *19*, 100591.

(28) Cárdenas-Arenas, A.; Soriano Cortés, H.; Bailón-García, E.; Davó-Quiñonero, A.; Lozano-Castelló, D.; Bueno-López, A. Active,

selective and stable NiO-CeO₂ nanoparticles for CO₂ methanation. *Fuel Process. Technol.* **2021**, *212*, 106637.

(29) Shanmugam, V.; Neuberger, S.; Zapf, R.; Pennemann, H.; Kolb, G. Effect of Support and Chelating Ligand on the Synthesis of Ni Catalysts with High Activity and Stability for CO₂ Methanation. *Catalysts* **2020**, *10*, 493.

(30) Wang, L.; Hu, J.; Liu, H.; Wei, Q.; Gong, D.; Mo, L.; Tao, H.; Zhang, C. Three-Dimensional Mesoporous Ni-CeO₂ Catalysts with Ni Embedded in the Pore Walls for CO₂ Methanation. *Catalysts* **2020**, *10*, 523.

(31) Rui, N.; Zhang, X.; Zhang, F.; Liu, Z.; Cao, X.; Xie, Z.; Zou, R.; Senanayake, S. D.; Yang, Y.; Rodriguez, J. A.; Liu, C.-J. Highly active Ni/CeO₂ catalyst for CO₂ methanation: Preparation and characterization. *Appl. Catal., B* **2021**, *282*, 119581.

(32) Bian, Z.; Chan, Y. M.; Yu, Y.; Kaw, S. Morphology dependence of catalytic properties of Ni/CeO₂ for CO₂ methanation: A kinetic and mechanism study. *Catal. Today* **2020**, *347*, 31–3832.

(33) Varvoutis, G.; Lykaki, M.; Stefa, S.; Papista, E.; Carabineiro, S. A.C.; Marnellos, G. E.; Konsolakis, M. Remarkable efficiency of Ni supported on hydrothermally synthesized CeO₂ nanorods for low-temperature CO₂ hydrogenation to methane. *Catal. Commun.* **2020**, *142*, 106036.

(34) Wang, F.; Li, C. M.; Zhang, X. Y.; Wei, M.; Evans, D. G.; Duan, X. Catalytic behavior of supported Ru nanoparticles on the {100}, {110}, and {111} facet of CeO₂. *J. Catal.* **2015**, *329*, 177–186.

(35) Sakpal, T.; Lefferts, L. Structure-dependent activity of CeO₂ supported Ru catalysts for CO₂ methanation. *J. Catal.* **2018**, *367*, 171–180.

(36) Zhu, M.; Tian, P.; Cao, X.; Chen, J.; Pu, T.; Shi, B.; Xu, J.; Moon, J.; Wu, Z.; Han, Y.-F. Vacancy engineering of the nickel-based catalysts for enhanced CO₂. *Appl. Catal., B* **2021**, *282*, 119561.

(37) Italiano, C.; Balzarotti, R.; Vita, A.; Latorrata, S.; Fabiano, C.; Pino, L.; Cristiani, C. Preparation of structured catalysts with Ni and Ni–Rh/CeO₂ catalytic layers for syngas production by biogas reforming processes. *Catal. Today* **2016**, *273*, 3–11.

(38) Palma, V.; Martino, M.; Truda, L. Nano-CeO₂ Coating on Aluminum Foam Carriers for Structured Catalysts Preparation. *Chem. Eng. Trans.* **2019**, *73*, 127–132.

(39) Vita, A.; Italiano, C.; Pino, L.; Frontera, P.; Ferraro, M.; Antonucci, V. Activity and stability of powder and monolith-coated Ni/GDC catalysts for CO₂ methanation. *Appl. Catal., B* **2018**, *226*, 384–395.

(40) Ho, P. H.; Ambrosetti, M.; Groppi, G.; Tronconi, E.; Jaroszewicz, J.; Ospitali, F.; Rodríguez-Castellón, E.; Fornasari, G.; Vaccari, A.; Benito, P. One-step electrodeposition of Pd–CeO₂ on high pore density foams for environmental catalytic processes. *Catal. Sci. Technol.* **2018**, *8*, 4678–4689.

(41) Ho, P. H.; Ambrosetti, M.; Groppi, G.; Tronconi, E.; Fornasari, G.; Vaccari, A.; Benito, P. Electrodeposition of CeO₂ and Pd–CeO₂ on small pore size metallic foams: Selection of deposition parameters. *Catal. Today* **2019**, *334*, 37–47.

(42) Basile, F.; Benito, P.; Fornasari, G.; Monti, M.; Scavetta, E.; Tonelli, D.; Vaccari, A. Novel Rh-based structured catalysts for the catalytic partial oxidation of methane. *Catal. Today* **2010**, *157*, 183–190.

(43) Ho, P. H.; Jabłońska, M.; Palkovits, R.; Rodríguez-Castellón, E.; Ospitali, F.; Fornasari, G.; Vaccari, A.; Benito, P. N₂O catalytic decomposition on electrodeposited Rh-based open-cell metallic foams. *Chem. Eng. J.* **2020**, *379*, 122259.

(44) Schilling, C.; Hofmann, A.; Hess, C.; Ganduglia-Pirovano, M. V. n. Raman Spectra of Polycrystalline CeO₂: A Density Functional Theory Study. *J. Phys. Chem. C* **2017**, *121*, 20834–20849.

(45) Popović, Z. V.; Dohčević-Mitrović, Z.; Konstantinović, M.; Šćepanović, M. Raman Scattering Characterization of Nanopowders and Nanowires (rods). *J. Raman Spectrosc.* **2007**, *38*, 750–755.

(46) Atzori, L.; Cutrufello, M. G.; Meloni, D.; Cannas, C.; Gazzoli, D.; Monaci, R.; Sini, M. F.; Rombi, E. Highly active NiO–CeO₂ catalysts for synthetic natural gas production by CO₂ methanation. *Catal. Today* **2018**, *299*, 183–192.

(47) Liu, Z.; Lu, Y.; Confer, M. P.; Cui, H.; Li, J.; Li, Y.; Wang, Y.; Street, S. C.; Wujcik, E. K.; Wang, R. Thermally Stable RuO_x–CeO₂ Nanofiber Catalysts for Low-Temperature CO Oxidation. *ACS Appl. Nano Mater.* **2020**, *3*, 8403–8413.

(48) Hall, D. S.; Lockwood, D. J.; Poirier, S.; Bock, C.; MacDougall, B. R. Applications of in Situ Raman Spectroscopy for Identifying Nickel Hydroxide Materials and Surface Layers during Chemical Aging. *ACS Appl. Mater. Interfaces* **2014**, *6* (5), 3141–3149.

(49) Liu, Z.; Lu, Y.; Confer, M. P.; Cui, H.; Li, J.; Li, Y.; Wang, Y.; Street, S. C.; Wujcik, E. K.; Wang, R. Thermally Stable RuO_x–CeO₂ Nanofiber Catalysts for Low-Temperature CO Oxidation. *ACS Appl. Nano Mater.* **2020**, *3*, 8403–8413.

(50) Atzori, L.; Cutrufello, M. G.; Meloni, D.; Monaci, R.; Cannas, C.; Gazzoli, D.; Sini, M. F.; Deiana, P.; Rombi, E. CO₂ methanation on hard-templated NiO single bond CeO₂ mixed oxides. *Int. J. Hydrogen Energy* **2017**, *42*, 20689–20702.

(51) Wang, W.; Liu, Y.; Xu, C.; Zheng, C.; Wang, G. Synthesis of NiO nanorods by a novel simple precursor thermal decomposition approach. *Chem. Phys. Lett.* **2002**, *362*, 119–122.

(52) Sartoretto, E.; Novara, C.; Giorgis, F.; Piumetti, M.; Bensaid, S.; Russo, N.; Fino, D. In situ Raman analyses of the soot oxidation reaction over nanostructured ceria-based catalysts. *Sci. Rep.* **2019**, *9*, 3875.

(53) Moretti, E.; Storaro, L.; Talon, A.; Moreno-Tost, R.; Rodríguez-Castellón, E.; Jiménez-López, A.; Lenarda, M. CO preferential oxidation activity of CuO/CeO₂ supported on zirconium doped MSU type silica. *Catal. Lett.* **2009**, *129*, 323–330.

(54) Moretti, E.; Lenarda, M.; Storaro, L.; Talon, A.; Frattini, R.; Reyes-Carmona, A.; Jiménez-López, A.; Rodríguez-Castellón, E. Influence of synthesis parameters on the performance of CeO₂–CuO and CeO₂–ZrO₂–CuO systems in the catalytic oxidation of CO in excess of hydrogen. *Appl. Catal., B* **2013**, *129*, 556–565.

(55) Zhang, F.; Wang, P.; Koberstein, J.; Khalid, S.; Chan, S. W. Cerium oxide state in ceria nanoparticles studied with X-ray photoelectron spectroscopy and adsorption near edge spectroscopy. *Surf. Sci.* **2004**, *563*, 74–82.

(56) Giordano, F.; Trovarelli, A.; de Leitenburg, C.; Giona, M. A Model for the Temperature-Programmed Reduction of Low and High Surface Area Ceria. *J. Catal.* **2000**, *193*, 273–282.

(57) Lee, S. M.; Lee, Y. H.; Moon, D. H.; Ahn, J. Y.; Nguyen, D. D.; Chang, S. W.; Kim, S. S. Reaction Mechanism and Catalytic Impact of Ni/CeO_{2-x} Catalyst for Low-Temperature CO₂ Methanation. *Ind. Eng. Chem. Res.* **2019**, *58*, 8656–8662.

(58) Shan, W.; Luo, M.; Ying, P.; Shen, W.; Li, C. Reduction property and catalytic activity of Ce_{1-x}Ni_xO₂ mixed oxide catalysts for CH₄ oxidation. *Appl. Catal., A* **2003**, *246*, 1–9.

(59) Ho, P. H.; Sanghez de Luna, G.; Angelucci, S.; Canciani, A.; Jones, W.; Decarolis, D.; Ospitali, F.; Rodríguez-Aguado, E.; Rodríguez-Castellón, E.; Fornasari, G.; Vaccari, A.; Beale, A. M.; Benito, P. Understanding structure-activity relationships in highly active La promoted Ni catalysts for CO₂ methanation. *Appl. Catal., B* **2020**, *278*, 119256.

(60) Yamada, K.; Ogo, S.; Yamano, R.; Higo, T.; Sekine, Y. Low-temperature Conversion of Carbon Dioxide to Methane in an Electric Field. *Chem. Lett.* **2020**, *49*, 303–306.

(61) Lin, S.; Hao, Z.; Shen, J.; Chang, X.; Huang, S.; Li, M.; Ma, X. Enhancing the CO₂ methanation activity of Ni/CeO₂ via activation treatment-determined metal-support interaction. *J. Energy Chem.* **2021**, *59*, 334–342.

(62) Mutschler, R.; Moiola, E.; Luo, W.; Gallandat, N.; Züttel, A. CO₂ hydrogenation reaction over pristine Fe, Co, Ni, Cu and Al₂O₃ supported Ru: Comparison and determination of the activation energies. *J. Catal.* **2018**, *366*, 139–149.